Letter

Incommensurate broken helix induced by nonstoichiometry in the axion insulator candidate $EuIn_2As_2$

Masaki Gen ,[1,2,*] Yukako Fujishiro,[1,3] Kazuki Okigami ,[4] Satoru Hayami ,[5] Max T. Birch,[1] Kiyohiro Adachi ,[6] Daisuke Hashizume ,[6] Takashi Kurumaji ,[7,8] Hajime Sagayama,[9] Hironori Nakao ,[9] Yoshinori Tokura,[1,3,10] and Taka-hisa Arima [1,7]

[1]*RIKEN Center for Emergent Matter Science (CEMS), Wako 351-0198, Japan*
[2]*Institute for Solid State Physics, University of Tokyo, Kashiwa, Chiba 277-8581, Japan*
[3]*RIKEN Cluster for Pioneering Research (CPR), Wako 351-0198, Japan*
[4]*Department of Applied Physics, University of Tokyo, Tokyo 113-8656, Japan*
[5]*Graduate School of Science, Hokkaido University, Sapporo 060-0810, Japan*
[6]*Materials Characterization Support Team, RIKEN Center for Emergent Matter Science (CEMS), Wako 351-0198, Japan*
[7]*Department of Advanced Materials Science, University of Tokyo, Kashiwa 277-8561, Japan*
[8]*Division of Physics, Mathematics and Astronomy, California Institute of Technology, Pasadena, California 91125, USA*
[9]*Institute of Materials Structure Science, High Energy Accelerator Research Organization, Tsukuba 305-0801, Japan*
[10]*Tokyo College, University of Tokyo, Tokyo 113-8656, Japan*

(Received 6 March 2024; revised 12 November 2024; accepted 3 February 2025; published 18 February 2025)

Zintl phase $EuIn_2As_2$ has garnered growing attention as an axion insulator candidate, triggered by the identification of a commensurate double-**Q** broken-helix state in previous studies, however, its periodicity and symmetry remain subjects of debate. Here, we perform resonant x-ray scattering experiments on $EuIn_2As_2$, revealing an incommensurate nature of the broken-helix state, where both the wave number and the amplitude of the helical modulation exhibit systematic sample dependence. Furthermore, the application of an in-plane magnetic field brings about a fanlike state that appears to preserve the double-**Q** nature, which might be attributed to multiple-spin interactions in momentum space. We propose that the itinerant character of $EuIn_2As_2$, most likely induced by Eu deficiency, gives rise to the helical modulation and impedes the realization of a theoretically predicted axion state with the collinear antiferromagnetic order.

DOI: 10.1103/PhysRevB.111.L081109

Europium-based compounds offer a fertile playground for exploring nontrivial magnetotransport phenomena [1–4]. In the presence of Fermi surfaces, the carrier-mediated Ruderman-Kittel-Kasuya-Yosida (RKKY) interaction can stabilize a variety of modulated magnetic structures such as helix [5–8] and skyrmions [9–13]. The correlation between magnetism and electronic band topology is one other intriguing aspect, as extensively studied in the 122 families of the Zintl phase [14–20]. First-principles calculations predict that $EuIn_2As_2$ can host an axion-insulating state (AXS) with the layered antiferromagnetic (AFM) order [21,22], thereby potentially exhibiting the quantized magnetoelectric effect [23–25]. Given that the AXS remains unestablished in stoichiometric bulk materials [25–30], a comprehensive investigation on the physical properties of $EuIn_2As_2$ stands as a critical issue [31–41], not only from the fundamental viewpoint but also for its applications in next-generation devices [23].

$EuIn_2As_2$ forms a hexagonal crystal structure with the space group $P6_3/mmc$, consisting of alternating stacks of Eu triangular layers and In_2As_2 blocks [Fig. 1(a)]. The theoretically predicted band structure is schematically illustrated in Fig. 1(b) [22,42]. There is a crossing of In 5*s* and As 4*p* bands near the Γ point, where a gap opens due to spin-orbit coupling. Although the Fermi energy is theoretically located in the band gap, angle-resolved photoemission spectroscopies (ARPESs) revealed holelike bulk bands crossing the Fermi level [33,34]. The magnetism is dominated by intraplane ferromagnetic and interplane AFM interactions between localized Eu^{2+} moments, with an easy-plane anisotropy becoming evident at low temperatures [32]. Neutron diffraction (ND) [39] and resonant x-ray scattering (RXS) experiments [40] observed a concurrent short-period magnetic modulation, $\mathbf{Q}_1 = (0, 0, q_{1z})$, along with the AFM component $\mathbf{Q}_2 = (0, 0, 1)$; the reported q_{1z} values are 0.303(1) [39] and 0.3328(6) [40], respectively, in the reciprocal-lattice unit. A phase separation scenario was excluded by azimuthal scans in the RXS [40]. Both studies proposed a six-layer-period double-**Q** helical structure, termed *broken helix*, under the assumption that $\mathbf{Q}_1$ represents an exactly commensurate modulation with $q_{1z} = 1/3$ [39,40]. Initially, the AXS was believed to be realized in the commensurate broken-helix state, as the $\mathcal{T}C_2$ symmetry (the combination of time-reversal and twofold rotational operations) is preserved once the principal axis of the broken helix is aligned along a specific crystallographic axis [39,40]. However, a recent optical birefringence study challenged the above picture in terms of the symmetry, and proposed the unpinned nature of the broken helix owing to minimal hexagonal anisotropy [41].

*Contact author: gen@issp.u-tokyo.ac.jp

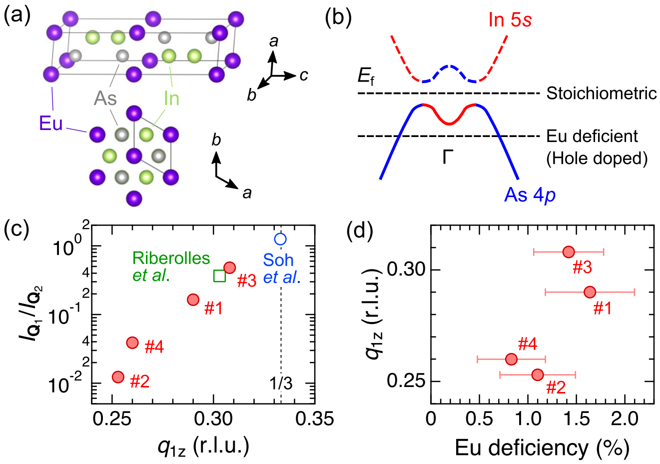

FIG. 1. (a) Crystal structure of Zintl phase $EuIn_2As_2$. The black line represents a crystallographic unit cell, which contains two Eu layers. (b) Schematic of the bulk band structure around the Γ point. The Fermi level is in the gap according to the first-principles calculations [22,42], although a hole pocket was observed in ARPESs [33,34]. (c) Relationship between the q_{1z} value and the integrated-intensity ratio of the $\mathbf{Q}_1$ to the $\mathbf{Q}_2$ peak $I_{\mathbf{Q}_1}/I_{\mathbf{Q}_2}$, observed for samples #1 ∼ #4 in this study (5 K) and those reported in Refs. [39,40] (6 K). See the SM [43] for the correction factors in estimating $I_{\mathbf{Q}_1}/I_{\mathbf{Q}_2}$. (d) Plots of the q_{1z} value versus Eu deficiency for samples #1 ∼ #4.

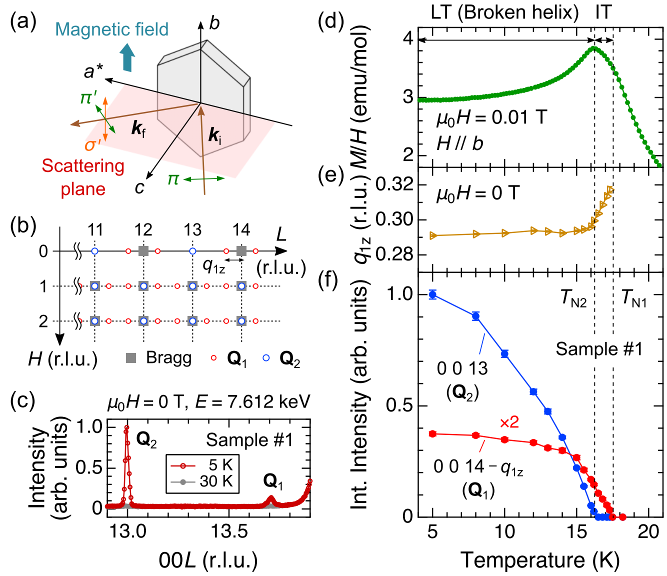

FIG. 2. (a) Experimental geometry of the RXS. $\mathbf{k}_i$ ($\mathbf{k}_f$) and π (π' and σ') represent the propagation vector and polarization direction of incident (scattered) x rays, respectively. (b) Positions of the Bragg peaks in the $(H, 0, L)$ scattering plane below T_{N2}. Gray squares are the fundamental peaks, and red (blue) open circles are the magnetic $\mathbf{Q}_1$ ($\mathbf{Q}_2$) peaks. (c) RXS profiles observed in the $(0, 0, L)$ scan at 5 K (red) and 30 K (gray) at zero field for sample #1. [(d)–(f)] Temperature dependence of (d) magnetic susceptibility M/H, (e) q_{1z}, and (f) integrated intensity of the $00L$ reflections with $L = 14 - q_{1z}$ (red) and $L = 13$ (blue) at zero field.

In this Letter, we reexamine the magnetic structure of $EuIn_2As_2$. While the preceding ND study identified an *incommensurate* $\mathbf{Q}_1$ modulation [39], no incommensurate spin configuration has been considered so far [39–41]. Whether $\mathbf{Q}_1$ is commensurate or not is pivotal, as the latter is not compatible with the AXS due to the $\mathcal{T}C_2$ symmetry breaking. The mechanism for the emergence of the $\mathbf{Q}_1$ modulation also remains puzzling [40,41]. To address these issues, we perform the RXS experiments, revealing that the $\mathbf{Q}_1$ peak exhibits variability in the q_{1z} value (0.25–0.31) as well as the intensity across samples [Fig. 1(c)]. The complementary single-crystal structure analyses reveal a greater amount of Eu deficiency for samples exhibiting a larger q_{1z} value [Fig. 1(d)]. These results suggest that the $\mathbf{Q}_1$ modulation stems from the RKKY interaction mediated by doped holes due to Eu deficiency. We argue that, to avoid the loss of generality, the broken-helix state should be considered as a superposition of incommensurate helical and collinear AFM modulations. The appearance of an exotic double-$\mathbf{Q}$ fanlike state is also revealed in an in-plane magnetic field.

Single crystals of $EuIn_2As_2$ were grown by an indium flux method. Details of sample growth and characterization are described in the Supplemental Material (SM) [43]. We picked up four specimens (#1 ∼ #4) from the same batch. RXS experiments were performed at BL-3A, Photon Factory, KEK, by using horizontally (π) polarized incident x rays in resonance with the Eu L_2 absorption edge ($E = 7.612$ keV) [7,11]. The incident x-ray beam was collimated with 1×1 mm^2, which is comparable or slightly larger than the sample size. Accordingly, the observed RXS intensity would come from almost all areas of the sample. Samples with the as-grown (001) plane were glued on an aluminum plate and set in a cryostat equipped with a vertical-field superconducting magnet. The scattering plane was set to be $(H, 0, L)$, and a magnetic field was applied along the crystallographic b axis [Fig. 2(a)]. We could access fundamental Bragg peaks at $(3m, 0, 2n)$ and $(3m \pm 1, 0, n)$ (m, n: integer), and their magnetic satellite peaks in the reciprocal space [Fig. 2(b)]. Unless otherwise stated, we performed the $(0, 0, L)$ scan with $L = 12$–16, and the scattered x rays were detected without analyzing the π' and σ' polarizations, parallel and perpendicular to the scattering plane, respectively. For polarization analysis, the 006 reflection of a pyrolytic graphite (PG) crystal was used, where the scattering angle was ∼92° near the Eu L_2 edge.

As in Refs. [39,40], we observe two kinds of magnetic Bragg peaks, $\mathbf{Q}_1 = (0, 0, q_{1z})$ and $\mathbf{Q}_2 = (0, 0, 1)$ [Fig. 2(c)]. Figures 2(d)–2(f) show the temperature dependence of magnetic susceptibility, q_{1z}, and integrated intensities of the $\mathbf{Q}_1$ and $\mathbf{Q}_2$ peaks at (nearly) zero field for sample #1. Upon cooling, the $\mathbf{Q}_1$ and $\mathbf{Q}_2$ peaks emerge below $T_{N1} = 17.6$ K and $T_{N2} = 16.2$ K, respectively. q_{1z} gradually decreases from 0.32 to 0.30 in the intermediate-temperature (IT) phase, while q_{1z} is almost temperature independent in the low-temperature (LT) phase, eventually reaching $q_{1z} = 0.29$ at 5 K. These features agree with Refs. [39,40], although there is a discrepancy in the q_{1z} value. Notably, distinct q_{1z} values are found for the other three samples: $q_{1z} = 0.25$, 0.31 and 0.26 for samples #2, #3, and #4, respectively (for additional RXS data, see the SM [43]). Besides, we find an important trend that the integrated intensity ratio of the $\mathbf{Q}_1$ peak to the $\mathbf{Q}_2$ peak, $I_{\mathbf{Q}_1}/I_{\mathbf{Q}_2}$, is higher for samples with larger q_{1z} [Fig. 1(c)]. We note that the way of adhering samples to the Al plate had little influence on

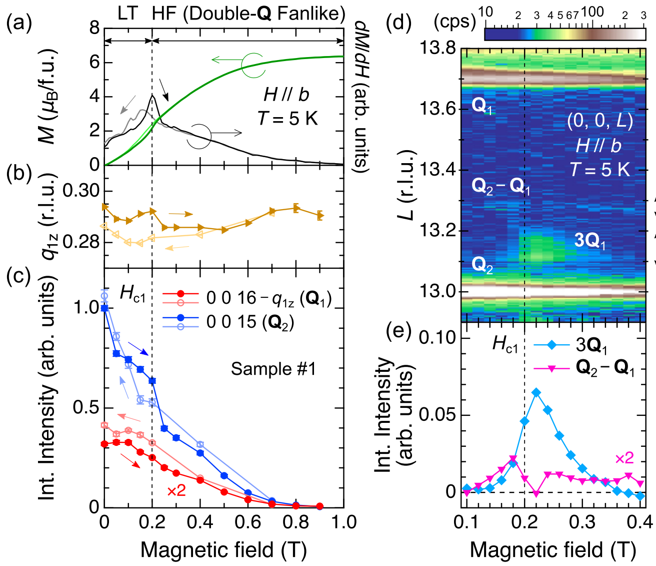

FIG. 3. [(a)–(c)] Magnetic-field dependence of (a) magnetization M (left axis) and its field derivative dM/dH (right axis), (b) q_{1z}, and (c) integrated intensity of the $00L$ reflections with $L = 16 - q_{1z}$ (red) and $L = 15$ (blue). Dark and light colors represent data in field increasing and decreasing processes, respectively. (d) Logarithmic contour plot of the RXS intensity in the $(0, 0, L)$ scan near H_{c1} in a field-increasing process. Black arrows on the right represent peak widths for $3\mathbf{Q}_1$ and $\mathbf{Q}_2 - \mathbf{Q}_1$. (e) Magnetic-field dependence of the integrated intensity of the $3\mathbf{Q}_1$ (cyan) and $\mathbf{Q}_2 - \mathbf{Q}_1$ (pink) peaks. The absolute value is normalized by the intensity of the 0013 reflection at 0 T. All the data are taken at 5 K with $H \parallel b$ for sample #1.

the RXS profile. Therefore, the observed variability in q_{1z} and $I_{\mathbf{Q}_1}/I_{\mathbf{Q}_2}$ appears to be primarily attributed to the sample dependence rather than extrinsic strain.

To confirm this from the structural point of view, we performed single-crystal x-ray diffraction experiments for all the four samples. Our crystal-structure analyses reveal the presence of a Eu deficiency of 1.64(46)%, 1.10(39)%, 1.42(36)%, and 0.83(35)% for samples #1 ∼ #4, respectively (for details, see the SM [43]). As shown in Fig. 1(d), one can see a trend that samples exhibiting a larger q_{1z} value host a greater amount of Eu deficiency. Recalling the first-principles calculations predicting a gapped insulating state with the AFM order characterized by $\mathbf{Q}_2$ [22], the additional $\mathbf{Q}_1$ modulation would be induced by doped hole carriers which contribute to the RKKY interaction between the Eu^{2+} moments. The above scenarios agree with the three-dimensional character of a hole pocket observed in a previous ARPES [33], although the details of the Fermi-surface shape need to be clarified. Indeed, our Hall resistivity measurements reveal the multicarrier nature, making the quantitative estimation of the carrier number challenging (see the SM [43]).

Next, we investigate the magnetic structure changes with the application of an in-plane magnetic field for sample #1 ($q_{1z} = 0.29$), which undergoes a metamagnetic transition at $\mu_0 H_{c1} = 0.2$ T at 5 K [32,35,40]. Figures 3(a)–3(c) show the field dependence of magnetization, q_{1z}, and integrated intensities of the $\mathbf{Q}_1$ and $\mathbf{Q}_2$ peaks. With increasing a magnetic field, both $\mathbf{Q}_1$ and $\mathbf{Q}_2$ peaks survive until the saturation field of 1.0 T. Here, q_{1z} exhibits only a small change of at most ±0.01 even across H_{c1}. With subsequently decreasing a magnetic field, a hysteresis appears around H_{c1} in the RXS profile, in line with the magnetization process. Ultimately, neither the intensities of the $\mathbf{Q}_1$ and $\mathbf{Q}_2$ peaks nor q_{1z} revert to the original values at zero field. The observed intensity changes against a magnetic field are qualitatively consistent with Ref. [40].

We find remarkable features in the RXS profile near H_{c1}. Figure 3(d) shows a logarithmic contour plot of the RXS intensity against a magnetic field, observed in the $(0, 0, L)$ scan in the L range between 12.9 and 13.8. Apart from the strong $\mathbf{Q}_1$ and $\mathbf{Q}_2$ peaks at $L = 13.71$ and 13, respectively, peaks around $L = 13.29$ and 13.13 are discernible in certain field ranges (for the RXS profile, see the SM [43]). These additional peaks likely correspond to higher-harmonic $\mathbf{Q}_2 - \mathbf{Q}_1$ and $3\mathbf{Q}_1$ modulations, respectively. The field evolution of integrated intensities of these peaks are displayed in Fig. 3(e). The weak $\mathbf{Q}_2 - \mathbf{Q}_1$ peak appears above 0.1 T and persists until at least 0.4 T, except immediately after H_{c1} where the intensity of the $3\mathbf{Q}_1$ peak becomes prominent. The presence of the $\mathbf{Q}_2 - \mathbf{Q}_1$ peak even above H_{c1} indicates the double-$\mathbf{Q}$ nature with a superposition of $\mathbf{Q}_1$ and $\mathbf{Q}_2$ in the high-field (HF) phase. We note that the $2\mathbf{Q}_1$ peak, expected in the conventional fanlike structure [48,49], is not observed at $L = 13.42$ in the entire field range, in spite of the observation of the $3\mathbf{Q}_1$ peak [Fig. 3(d)]. This also rules out the possibility of the presence of a single-$\mathbf{Q}$ fanlike state in the HF phase.

To get information on the orientation of magnetic moments in each phase at 5 K, we performed polarization analysis with $H \parallel b$. In general, the magnetic scattering intensity I is given by $I \propto |(\mathbf{e}_i \times \mathbf{e}_f) \cdot \mathbf{m}_\mathbf{Q}|^2$, where $\mathbf{e}_i$ ($\mathbf{e}_f$) is the polarization vector of the incident (scattered) beam, and $\mathbf{m}_\mathbf{Q}$ is a magnetic moment of the $\mathbf{Q}$ modulation. The π–π' channel ($I_{\pi-\pi'}$) always detects the modulated component along b (m_b), whereas the π–σ' channel ($I_{\pi-\sigma'}$) contains those along a^* (m_{a^*}) and c (m_c) in the ratio of $\cos^2\omega : \sin^2\omega$, where ω is the angle between the propagation vector of the incident beam ($\mathbf{k}_i$) and the a^* axis. Figures 4(a) and 4(b) show the experimental configurations of polarization analysis focusing on the Bragg spots at $(-2, 0, 11.71)$ and $(0, 0, 9)$, in which $I_{\pi-\sigma'}$ mainly reflects m_{a^*} (∼100% and 83%) of the $\mathbf{Q}_1$ and $\mathbf{Q}_2$ modulations, respectively. The results are summarized in Figs. 4(c)–4(h). Additional measurements focusing on the Bragg spots at $(2, 0, 11.71)$ and $(0, 0, 17)$ confirm the absence of m_c (see the SM [43]), i.e., all the spins lie within the ab plane.

At zero field, both $I_{\pi-\pi'}$ and $I_{\pi-\sigma'}$ have intensities at $(-2, 0, 11.71)$ and $(0, 0, 9)$ [Figs. 4(c) and 4(f)]. At 0.1 T ($< H_{c1}$), a drastic enhancement is observed in $I_{\pi-\sigma'}$ at $(0, 0, 9)$, accompanied by a suppression of $I_{\pi-\pi'}$ [Fig. 4(g)], suggesting the reorientation of magnetic domains so as to lie the AFM component perpendicular to the field direction. In contrast, $I_{\pi-\pi'}$ and $I_{\pi-\sigma'}$ still have comparable intensities at $(-2, 0, 11.71)$ [Fig. 4(d)]. This observation suggests that the $\mathbf{Q}_1$ peak originates from a helical modulation rather than a sinusoidal one, as the intensity should appear only in either $I_{\pi-\pi'}$ or $I_{\pi-\sigma'}$ in the latter case. Followed by the metamagnetic transition, the presence of only m_{a^*} is confirmed for both the $\mathbf{Q}_1$ and $\mathbf{Q}_2$ modulations, as evidenced by the disappearance of $I_{\pi-\pi'}$ at both Bragg positions at 0.3 T ($> H_{c1}$) [Figs. 4(e) and 4(h)]. Accordingly, the HF phase can be ascribed to a double-$\mathbf{Q}$ fanlike state.

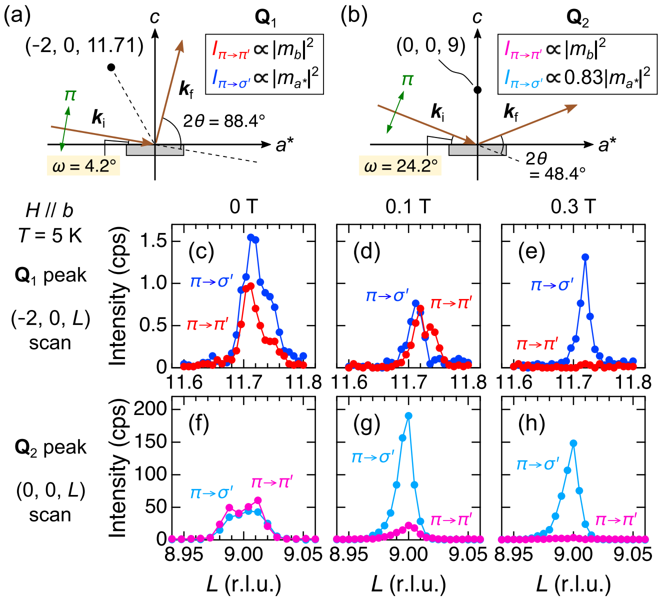

FIG. 4. [(a),(b)] Schematic geometrical configuration of the RXS focusing on the $\mathbf{Q}_1$ and $\mathbf{Q}_2$ peaks around the magnetic Bragg spots $(-2, 0, 11.71)$ and $(0, 0, 9)$, respectively. See also Figs. 2(a) and 2(b). [(c)–(h)] RXS profiles of the polarization analysis at 5 K at 0 T [(c),(f)], 0.1 T [(d),(g)], and 0.3 T [(e),(h)] with $H \parallel b$. Panels (c)–(e) and (f)–(h) show the data of the $(-2, 0, L)$ scan around $L = 11.71$ and the $(0, 0, L)$ scan around $L = 9$, respectively.

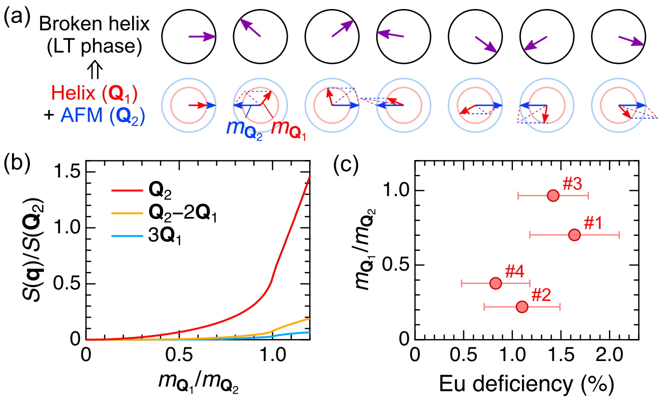

FIG. 5. (a) Schematic of the broken-helix state and an equivalent double-**Q** representation as the superposition of incommensurate helical $\mathbf{Q}_1$ and collinear AFM $\mathbf{Q}_2$ modulations. Magnetic moments are in the *ab* plane, and the modulation is along the *c* axis. (b) $m_{\mathbf{Q}_1}/m_{\mathbf{Q}_2}$ dependence of the spin-structure factor $S(\mathbf{q})$ relative to $S(\mathbf{Q}_2)$ at $\mathbf{Q}_1$, $\mathbf{Q}_2 - 2\mathbf{Q}_1$, and $3\mathbf{Q}_1$. The $S(\mathbf{q})$ profiles exhibit an anomaly at a singular point $m_{\mathbf{Q}_1}/m_{\mathbf{Q}_2} = 1$, where the antiparallel $m_{\mathbf{Q}_1}$ and $m_{\mathbf{Q}_2}$ moments cancel each other out. (c) Relationship between Eu deficiency and a moment-amplitude ratio of the $\mathbf{Q}_1 = (0, 0, q_{1z})$ to the $\mathbf{Q}_2 = (0, 0, 1)$ modulation, $m_{\mathbf{Q}_1}/m_{\mathbf{Q}_2}$, in the broken-helix state for samples #1 $\sim$ #4.

Let us here update the understanding of the magnetic structure in $EuIn_2As_2$. Our RXS experiments suggest that the LT phase is a broken-helix state with a superposition of incommensurate helical $\mathbf{Q}_1$ and AFM $\mathbf{Q}_2$ modulation [Fig. 5(a)], which can be approximately described as $\mathbf{S}_i = \mathbf{m}(\mathbf{r}_i)/|\mathbf{m}(\mathbf{r}_i)|$, where $\mathbf{m}(\mathbf{r}_i) \propto (1, i, 0) \sum_{\eta=1,2} m_{\mathbf{Q}_\eta} \exp(i\mathbf{Q}_\eta \cdot \mathbf{r}_i) + \text{c.c.}$ at zero field. This expression encompasses the commensurate broken helix proposed in Refs. [39,40] as a special case. Based on the above formula, we calculate the spin-structure factor $S(\mathbf{q}) = (1/N) \sum_{i,j} \langle \mathbf{S}_i \cdot \mathbf{S}_j \rangle e^{i\mathbf{q}(\mathbf{r}_i - \mathbf{r}_j)}$ at $\mathbf{Q}_1$ and $\mathbf{Q}_2$ as a function of $m_{\mathbf{Q}_1}/m_{\mathbf{Q}_2}$, as shown in Fig. 5(b) [50]. By comparing the calculated $S(\mathbf{Q}_1)/S(\mathbf{Q}_2)$ with the observed intensity ratio $I_{\mathbf{Q}_1}/I_{\mathbf{Q}_2}$ [Fig. 1(c)], we estimate $m_{\mathbf{Q}_1}/m_{\mathbf{Q}_2}$ at the lowest temperature for each sample used in this study, as shown in Fig. 5(c) (for details, see the SM [43]). A positive correlation between the Eu deficiency and $m_{\mathbf{Q}_1}/m_{\mathbf{Q}_2}$ agrees with the RKKY picture for the emergence of helimagnetism by hole doping, as mentioned above. Furthermore, our simulation of $S(\mathbf{q})$ for the broken-helix state indicates the appearance of weak higher-harmonic peaks at $\mathbf{Q}_2 - 2\mathbf{Q}_1$ and $3\mathbf{Q}_1$ [Fig. 5(b)], although we could not confirm their presence in the RXS experiments at zero field. We note that the IT phase was identified as a sinusoidal state by Mössbauer [39] and optical birefringence measurements [41]. As the hexagonal anisotropy is negligibly weak [32,41], the sinusoidal modulation would be stabilized by thermal fluctuations and gradually transforms into helix with decreasing temperature. We thus infer that in the LT phase at 5 K, there is a slight elliptical distortion of the helix component, leading to the suppression of the higher harmonics.

Our RXS experiments also suggest a helix-fan transition while keeping the double-**Q** nature in an in-plane magnetic field, as indicated by the observation of higher harmonics $\mathbf{Q}_2 - \mathbf{Q}_1$ and $3\mathbf{Q}_1$, along with the absence of $2\mathbf{Q}_1$. There have been reports of other Eu-based itinerant magnets exhibiting the coexistence of two magnetic modulations along the *c* axis, such as $EuRh_2As_2$ [5], EuCuSb [6], and EuZnGe [7], although their microscopic origins, as well as field-induced magnetic structure changes, are not yet fully understood. Accordingly, it is crucial to establish theoretical approaches for a better understanding of the complex helimagnetism characterized by double-**Q** interplane modulations. Here, we investigate several types of spin models, aiming to reproduce the field-induced phase transition in $EuIn_2As_2$. The detailed calculation results are presented in the SM [43], and in the following, we briefly describe our updated knowledge.

Donoway *et al.* proposed a spin Hamiltonian composed of long-range Heisenberg exchange and biquadratic exchange interactions in real space on a one-dimensional chain [41]. Through simulated annealing, we find that this model can stabilize an incommensurate broken helix with a dominant $\mathbf{Q}_2$ component at zero field. When applying an in-plane magnetic field, however, it fails to preserve the double-**Q** nature and instead stabilizes a canted AFM state. Alternatively, an effective spin Hamiltonian composed of bilinear and biquadratic exchange interactions in momentum space [51] can yield qualitative agreement with the experimental observations, provided that some additional terms are introduced: (i) an intertwined exchange coupling term $-K_2(\mathbf{S}_{\mathbf{Q}_1} \cdot \mathbf{S}_{\mathbf{Q}_2})(\mathbf{S}_{-\mathbf{Q}_1} \cdot \mathbf{S}_{-\mathbf{Q}_2})$, and (ii) higher-harmonic exchange coupling terms $-J''\mathbf{S}_{3\mathbf{Q}_1} \cdot \mathbf{S}_{-3\mathbf{Q}_1}$ and $K''(\mathbf{S}_{3\mathbf{Q}_1} \cdot \mathbf{S}_{-3\mathbf{Q}_1})^2$, where $K_2, J'', K'' > 0$. These terms (i) and (ii) are necessary to stabilize a double-**Q** fanlike state and to enhance the $3\mathbf{Q}_1$ modulation, respectively, in high magnetic fields. The resultant magnetic structure exhibits a peculiar feature of the double-**Q** fanlike state. Immediately after the metamagnetic transition, a square-wave-shaped modulation appears perpendicular to the field direction, reflecting the effect of $3\mathbf{Q}_1$ along with $\mathbf{Q}_1$. In higher magnetic fields, where the $3\mathbf{Q}_1$ modulation diminishes, the spin configuration transforms into a conventional fanlike state, while the remaining $\mathbf{Q}_2$ component contributes to a complex spin-flipping pattern.

In summary, we elucidate the incommensurate nature of the double-**Q** broken-helix state in $EuIn_2As_2$ through RXS experiments, contradicting the previously proposed commensurate broken helix [39,40]. Furthermore, we observe the possible emergence of a double-**Q** fanlike state with higher-harmonic modulations in an in-plane magnetic field. The double-**Q** nature likely arises from the RKKY mechanism via hole carriers introduced by Eu deficiency. To verify this scenario, further detailed studies on multiple samples, including ARPES, magnetotransport measurements, and extended x-ray absorption fine-structure analysis would be beneficial. Our study indicates that the modulation period of the helix component is an excellent indicator for evaluating the sample quality of $EuIn_2As_2$. We propose that electron doping in *off-stoichiometric* $EuIn_2As_2$ through chemical substitution can be a promising pathway to shift the Fermi energy to the band gap and suppress the helical modulation, realizing the theoretically predicted AXS with the collinear AFM order [22].

This work was financially supported by the JSPS KAKENHI Grants-In-Aid for Scientific Research (Grants No. 22H00101, No. 22K14011, No. 23H04869, No. 23H05431, and No. 23K13068), JST SPRING (Grant No. JPMJSP2108), and JST PRESTO (Grant No. MJPR20L8). The resonant x-ray scattering experiments were performed with the approval of the Photon Factory Program Advisory Committee (Proposals No. 2022G551 and No. 2023G093). The authors appreciate A. Kikkawa and M. Kriener for the invaluable support in the synthesis of the single crystals used in this study. The authors appreciate H. Takeda, S. Kitou, M. Hirschberger, and K. Kakurai for fruitful discussions.

[1] G. A. Wigger, C. Beeli, E. Felder, H. R. Ott, A. D. Bianchi, and Z. Fisk, Percolation and the colossal magnetoresistance of Eu-based hexaboride, Phys. Rev. Lett. **93**, 147203 (2004).

[2] K. Kawashima, T. Kinjo, T. Nishio, S. Ishida, H. Fujihisa, Y. Gotoh, K. Kihou, H. Eisaki, Y. Yoshida, and A. Iyo, Superconductivity in Fe-based compound $EuAFe_4As_4$ (A = Rb and Cs), J. Phys. Soc. Jpn. **85**, 064710 (2016).

[3] P. Rosa, Y. Xu, M. Rahn, J. Souza, S. Kushwaha, L. Veiga, A. Bombardi, S. Thomas, M. Janoschek, E. Bauer, M. Chan, Z. Wang, J. Thompson, N. Harrison, P. Pagliuso, A. Bernevig, and F. Ronning, Colossal magnetoresistance in a nonsymmorphic antiferromagnetic insulator, npj Quantum Mater. **5**, 52 (2020).

[4] A. H. Mayo, H. Takahashi, M. S. Bahramy, A. Nomoto, H. Sakai, and S. Ishiwata, Magnetic generation and switching of topological quantum phases in a trivial semimetal α-EuP_3, Phys. Rev. X **12**, 011033 (2022).

[5] S. Nandi, A. Kreyssig, Y. Lee, Y. Singh, J. W. Kim, D. C. Johnston, B. N. Harmon, and A. I. Goldman, Magnetic ordering in $EuRh_2As_2$ studied by x-ray resonant magnetic scattering, Phys. Rev. B **79**, 100407(R) (2009).

[6] H. Takahashi, K. Aono, Y. Nambu, R. Kiyanagi, T. Nomoto, M. Sakano, K. Ishizaka, R. Arita, and S. Ishiwata, Competing spin modulations in the magnetically frustrated semimetal EuCuSb, Phys. Rev. B **102**, 174425 (2020).

[7] T. Kurumaji, M. Gen, S. Kitou, H. Sagayama, A. Ikeda, and T.-h. Arima, Anisotropic magnetotransport properties coupled with spiral spin modulation in a magnetic semimetal EuZnGe, Phys. Rev. Mater. **6**, 094410 (2022).

[8] J.-R. Soh, I. S. Ramírez, X. Yang, J. Sun, I. Zivkovic, J. A. R.-Velamazán, O. Fabelo, A. Stunault, A. Bombardi, C. Balz, M. D. Le, H. C. Walker, J. H. Dil, D. Prabhakaran, H. M. Rønnow, F. de Juan, M. G. Vergniory, and A. T. Boothroyd, Weyl metallic state induced by helical magnetic order, npj Quantum Mater. **9**, 7 (2024).

[9] K. Kaneko, M. D. Frontzek, M. Matsuda, A. Nakao, K. Munakata, T. Ohhara, M. Kakihana, Y. Haga, M. Hedo, T. Nakama, and Y. Ōnuki, Unique helical magnetic order and field-induced phase in trillium lattice antiferromagnet EuPtSi, J. Phys. Soc. Jpn. **88**, 013702 (2019).

[10] R. Takagi, N. Matsuyama, V. Ukleev, L. Yu, J. S. White, S. Francoual, J. R. L. Mardegan, S. Hayami, H. Saito, K. Kaneko, K. Ohishi, Y. Ōnuki, T.-h. Arima, Y. Tokura, T. Nakajima, and S. Seki, Square and rhombic lattices of magnetic skyrmions in a centrosymmetric binary compound, Nat. Commun. **13**, 1472 (2022).

[11] M. Gen, R. Takagi, Y. Watanabe, S. Kitou, H. Sagayama, N. Matsuyama, Y. Kohama, A. Ikeda, Y. Ōnuki, T. Kurumaji, T.-h. Arima, and S. Seki, Rhombic skyrmion lattice coupled with orthorhombic structural distortion in $EuAl_4$, Phys. Rev. B **107**, L020410 (2023).

[12] D. Singh, Y. Fujishiro, S. Hayami, S. H. Moody, T. Nomoto, P. R. Baral, V. Ukleev, R. Cubitt, N.-J. Steinke, D. J. Gawryluk, E. Pomjakushina, Y. Ōnuki, R. Arita, Y. Tokura, N. Kanazawa, and J. S. White, Transition between distinct hybrid skyrmion textures through their hexagonal-to-square crystal transformation in a polar magnet, Nat. Commun. **14**, 8050 (2023).

[13] T. Matsumura, K. Kurauchi, M. Tsukagoshi, N. Higa, H. Nakao, M. Kakihana, M. Hedo, T. Nakama, and Y. Ōnuki, Helicity unification by triangular skyrmion lattice formation in the noncentrosymmetric tetragonal magnet $EuNiGe_3$, J. Phys. Soc. Jpn. **93**, 074705 (2024).

[14] J. Jiang and S. M. Kauzlarich, Colossal magnetoresistance in a rare earth zintl compound with a new structure type: $EuIn_2P_2$, Chem. Mater. **18**, 435 (2006).

[15] J.-Z. Ma, S. M. Nie, C. J. Yi, J. Jandke, T. Shang, M. Y. Yao, M. Naamneh, L. Q. Yan, Y. Sun, and A. Chikina *et al.*, Spin fluctuation induced weyl semimetal state in the paramagnetic phase of $EuCd_2As_2$, Sci. Adv. **5**, eaaw4718 (2019).

[16] H. Su, B. Gong, W. Shi, H. Yang, H. Wang, W. Xia, Z. Yu. P.-J. Guo, J. Wang, L. Ding, L. Xu, X. Li, X. Wang, Z. Zou, N. Yu, Z. Zhu, Y. Chen, Z. Liu, K. Liu, G. Li, and Y. Guo, Magnetic exchange induced Weyl state in a semimetal $EuCd_2Sb_2$, APL Mater. **8**, 011109 (2020).

[17] Z.-C. Wang, J. D. Rogers, X. Yao, R. Nichols, K. Atay, B. Xu, J. Franklin, I. Sochnikov, P. J. Ryan, D. Haskel, and F. Taft, Colossal magnetoresistance without mixed valence in a layered phosphide crystal, Adv. Mater. **33**, 2005755 (2021).

[18] J. Blawat, M. Marshall, J. Singleton, E. Feng, H. Cao, W. Xie, and R. Jin, Unusual electrical and magnetic properties in layered $EuZn_2As_2$, Adv. Quantum Tech. **5**, 2200012 (2022).

[19] S. Krebber, M. Kopp, C. Garg, K. Kummer, J. Sichelschmidt, S. Schulz, G. Poelchen, M. Mende, A. V. Virovets, K. Warawa, M. D. Thomson, A. V. Tarasov, D. Yu. Usachov, D. V. Vyalikh, H. G. Roskos, J. Müller, C. Krellner, and K. Kliemt, Colossal magnetoresistance in $EuZn_2P_2$ and its electronic and magnetic structure, Phys. Rev. B **108**, 045116 (2023).

[20] G. Cuono, R. M. Sattigeri, C. Autieri, and T. Dietl, *Ab initio* overestimation of the topological region in Eu-based compounds, Phys. Rev. B **108**, 075150 (2023).

[21] A. M. Essin, J. E. Moore, and D. Vanderbilt, Magnetoelectric polarizability and axion electrodynamics in crystalline insulators, Phys. Rev. Lett. **102**, 146805 (2009).

[22] Y. Xu, Z. Song, Z. Wang, H. Weng, and X. Dai, Higher-Order topology of the axion insulator $EuIn_2As_2$, Phys. Rev. Lett. **122**, 256402 (2019).

[23] Y. Tokura, K. Yasuda, and A. Tsukazaki, Magnetic topological insulators, Nat. Rev. Phys. **1**, 126 (2019).

[24] B. A. Bernevig, C. Felser, and H. Beidenkopf, Progress and prospects in magnetic topological materials, Nature (London) **603**, 41 (2022).

[25] K. M. Fijalkowski, N. Liu, M. Hartl, M. Winnerlein, P. Mandal, A. Coschizza, A. Fothergill, S. Grauer, S. Schreyeck, K. Brunner, M. Greiter, R. Thomale, C. Gould, and L. W. Molenkamp, Any axion insulator must be a bulk three-dimensional topological insulator, Phys. Rev. B **103**, 235111 (2021).

[26] X. Wan, A. M. Turner, A. Vishwanath, and S. Y. Savrasov, Topological semimetal and Fermi-arc surface states in the electronic structure of pyrochlore iridates, Phys. Rev. B **83**, 205101 (2011).

[27] M. Mogi, M. Kawamura, R. Yoshimi, A. Tsukazaki, Y. Kozuka, N. Shirakawa, K. S. Takahashi, M. Kawasaki, and Y. Tokura, A magnetic heterostructure of topological insulators as a candidate for an axion insulator, Nat. Mater. **16**, 516 (2017).

[28] D. Zhang, M. Shi, T. Zhu, D. Xing, H. Zhang, and J. Wang, Topological axion states in the magnetic insulator $MnBi_2Te_4$ with the quantized magnetoelectric effect, Phys. Rev. Lett. **122**, 206401 (2019).

[29] J. Li, Y. Li, S. Du, Z. Wang, B.-L. Gu, S.-C. Zhang, K. He, W. Duan, and Y. Xu, Intrinsic magnetic topological insulators in van der Waals layered $MnBi_2Te_4$-family materials, Sci. Adv. **5**, eaaw5685 (2019).

[30] Y. Deng, Y. Yu, M. Z. Shi, Z. Guo, Z. Xu, J. Wang, X. H. Chen, Y. Zhang, Quantum anomalous Hall effect in intrinsic magnetic topological insulator $MnBi_2Te_4$, Science **367**, 895 (2020).

[31] A. M. Goforth, P. Klavins, J. C. Fettinger, and S. M. Kauzlarich, Magnetic properties and negative colossal magnetoresistance of the rare earth zintl phase $EuIn_2As_2$, Inorg. Chem. **47**, 11048 (2008).

[32] Y. Zhang, K. Deng, X. Zhang, M. Wang, Y. Wang, C. Liu, J.-W. Mei, S. Kumar, E. F. Schwier, K. Shimada, C. Chen, and B. Shen, In-plane antiferromagnetic moments and magnetic polaron in the axion topological insulator candidate $EuIn_2As_2$, Phys. Rev. B **101**, 205126 (2020).

[33] T. Sato, Z. Wang, D. Takane, S. Souma, C. Cui, Y. Li, K. Nakayama, T. Kawakami, Y. Kubota, C. Cacho, T. K. Kim, A. Arab, V. N. Strocov, Y. Yao, and T. Takahashi, Signature of band inversion in the antiferromagnetic phase of axion insulator candidate $EuIn_2As_2$, Phys. Rev. Res. **2**, 033342 (2020).

[34] S. Regmi, M. M. Hosen, B. Ghosh, B. Singh, G. Dhakal, C. Sims, B. Wang, F. Kabir, K. Dimitri, Y. Liu, A. Agarwal, H. Lin, D. Kaczorowski, A. Bansil, and M. Neupane, Temperature-dependent electronic structure in a higher-order topological insulator candidate $EuIn_2As_2$, Phys. Rev. B **102**, 165153 (2020).

[35] F. H. Yu, H. M. Mu, W. Z. Zhuo, Z. Y. Wang, Z. F. Wang, J. J. Ying, and X. H. Chen, Elevating the magnetic exchange coupling in the compressed antiferromagnetic axion insulator candidate $EuIn_2As_2$, Phys. Rev. B **102**, 180404(R) (2020).

[36] M. Gong, D. Sar, J. Friedman, D. Kaczorowski, S. A. Razek, W.-C. Lee, and P. Aynajian, Surface state evolution induced by magnetic order in axion insulator candidate $EuIn_2As_2$, Phys. Rev. B **106**, 125156 (2022).

[37] J. Yan, Z. Z. Jiang, R. C. Xiao, W. J. Lu, W. H. Song, X. B. Zhu, X. Luo, Y. P. Sun, and M. Yamashita, Field-induced topological Hall effect in antiferromagnetic axion insulator candidate $EuIn_2As_2$, Phys. Rev. Res. **4**, 013163 (2022).

[38] Q. Wu, T. Hu, D. Wu, R. Li, L. Yue, S. Zhang, S. Xu, Q. Liu, T. Dong, and N. Wang, Spin dynamics in the axion insulator candidate $EuIn_2As_2$, Phys. Rev. B **107**, 174411 (2023).

[39] S. X. M. Riberolles, T. V. Trevisan, B. Kuthanazhi, T. W. Heitmann, F. Ye, D. C. Johnston, S. L. Bud'ko, D. H. Ryan, P. C. Canfield, A. Kreyssig, A. Vishwanath, R. J. McQueeney, L.-L. Wang, P. P. Orth, and B. G. Ueland, Magnetic crystalline-symmetry-protected axion electrodynamics and field-tunable unpinned Dirac cones in $EuIn_2As_2$, Nat. Commun. **12**, 999 (2021).

[40] J.-R. Soh, A. Bombardi, F. Mila, M. C. Rahn, D. Prabhakaran, S. Francoual, H. M. Rønnow, and A. T. Boothroyd, Understanding unconventional magnetic order in a candidate axion insulator by resonant elastic x-ray scattering, Nat. Commun. **14**, 3387 (2023).

[41] E. Donoway, T. V. Trevisan, A. Liebman - Peláez, R. P. Day, K. Yamakawa, Y. Sun, J. R. Soh, D. Prabhakaran, A. Boothroyd, R. M. Fernandes, J. G. Analytis, J. E. Moore, J. Orenstein, and V. Sunko, Symmetry-breaking pathway towards the unpinned broken helix, Phys. Rev. X **14**, 031013 (2024).

[42] W. Cao, H. Yang, Y. Li, C. Pei, Q. Wang, Y. Zhao, C. Li, M. Zhang, S. Zhu, J. Wu, L. Zhang, Z. Wang, Y. Yao, Z. Liu, Y. Chen, and Y. Qi, Pressure-induced superconductivity in the Zintl topological insulator $SrIn_2As_2$, Phys. Rev. B **108**, 224510 (2023).

[43] See Supplemental Material at http://link.aps.org/supplemental/10.1103/PhysRevB.111.L081109 for details of the experiments and analyses, which includes Refs. [44–47].

[44] F. Izumi and K. Momma, Three-dimensional visualization in powder diffraction, Solid State Phenom. **130**, 15 (2007).

[45] CrysAlisPro (Agilent Technologies Ltd, Yarnton, 2014).

[46] V. Petříček, M. Dušek, and L. Palatinus, Crystallographic computing system JANA2006: General features, Z. Kristallogr. Cryst. Mater. **229**, 345 (2014).

[47] I. Isenberg, B. R. Russell, and R. F. Greene, Improved method for measuring Hall coefficients, Rev. Sci. Instrum. **19**, 685 (1948).

[48] T. Kosugia, S. Kawanob, N. Achiwac, A. Onoderad, Y. Nakaie, and N. Yamamoto, Direct evidence of helifan structures in holmium by single crystal neutron diffraction, Physica B: Condens. Matter **334**, 365 (2003).

[49] N. J. Ghimire, R. L. Dally, L. Poudel, D. C. Jones, D. Michel, N. T. Magar, M. Bleuel, M. A. McGuire, J. S. Jiang, J. F. Mitchell, J. W. Lynn, and I. I. Mazin, Competing magnetic phases and fluctuation-driven scalar spin chirality in the kagome metal YMn_6Sn_6, Sci. Adv. **6**, eabe2680 (2020).

[50] Note that the relation between $S(\mathbf{q})/S(\mathbf{Q}_2)$ and $m_{\mathbf{Q}_1}/m_{\mathbf{Q}_2}$ does not depend on the q_{1z} value.

[51] S. Hayami, R. Ozawa, and Y. Motome, Effective bilinear-biquadratic model for noncoplanar ordering in itinerant magnets, Phys. Rev. B **95**, 224424 (2017).